

Opportunities and Challenges in MOCVD of β -Ga₂O₃ for Power Electronic Devices

M. A. Mastro*, J. K. Hite, C. R. Eddy, Jr., and M. J. Tadje

U.S. Naval Research Laboratory, Washington, DC 20375, USA

*michael.mastro@nrl.navy.mil

S. J. Pearton

*Department of Materials Science and Engineering, University of Florida,
Gainesville, FL 32611, USA*

F. Ren

*Department of Chemical Engineering, University of Florida,
Gainesville, FL 32611, USA*

J. Kim

*Department of Chemical and Biological Engineering, Korea University,
Seoul 02841, Korea*

Received 1 August 2019

Accepted 26 August 2019

Recent breakthroughs in bulk crystal growth of β -Ga₂O₃ by the edge-defined film-fed technique has led to the commercialization of large-area β -Ga₂O₃ substrates. Standard epitaxy approaches are being utilized to develop various thin-film β -Ga₂O₃ based devices including lateral transistors. This article will discuss the challenges for metal organic chemical vapor deposition (MOCVD) of β -Ga₂O₃ and the design criteria for use of this material system in power electronic device structures.

Keywords: Gallium oxide; MOCVD; power electronic device.

1. Properties

β -Ga₂O₃-based transistors and diodes possess fundamental electronic properties that make them ideal candidates for high power devices (Table 1). A number of these properties derive directly from the wide band-gap of β -Ga₂O₃ ($E_g = 4.85$ eV) including an exceptionally high electric breakdown field (approximately 8 MV/cm). This high breakdown field allows β -Ga₂O₃-based devices to be biased at a high drain voltage ($V_{\text{break-down}} \gg 10$ kV) while maintaining a large dynamic range. Furthermore, the wide band-gap of β -Ga₂O₃ allows device operation at elevated temperature without degradation. Additionally, Ga₂O₃ has a high saturation electron velocity ($v_{\text{sat}} = 2 \times 10^7$ cm/s), which is partially accountable for the high current density, I_{max} (where $I_{\text{max}} \approx qnv_{\text{sat}}$, q is the elementary charge, and n is the charge density) in devices [1].

Table 1. Properties of relevant semiconductor materials and normalized unipolar power-device figures of merit (FOM). The Johnson FOM describes the power-frequency capability, the Baliga FOM gives the specific on-resistance in the drift region, the combined FOM combines the power, frequency, voltage metrics, the Baliga high-frequency FOM provides a measure of switching losses, the Keyes FOM describes the thermal capability to handle high power density at high frequency. The Johnson and Baliga FOMs are remarkably high for Ga_2O_3 [2].

<u>Properties</u>	Si	GaAs	Diamond	4H-SiC	GaN	Ga_2O_3
Bandgap E_g [eV]	1.12	1.42	5.5	3.25	3.4	4.85
Dielectric Constant, ϵ	11.8	12.9	5.7	9.7	9	10
Breakdown Field, E_c [MV/cm]	0.3	0.4	20	2.5	3.3	8
Electron Mobility, μ [$\text{cm}^2/\text{V}\cdot\text{s}$]	1500	8500	4500	1000	1250	250
Maximum Velocity, v_s [10^7 cm/s]	1	1	2.5	2	3	2
Thermal Conductivity, λ , [W/cm·K]	1.5	0.5	24	4.9	2.3	0.23
<u>Figure of Merits / relative to Si</u>						
Johnson = $E_c^2 \cdot V_s^2 / 4\pi^2$	1	1.8	27777	277	1089	2844
Baliga = $\epsilon \cdot \mu \cdot E_c^3$	1	14.7	429378	317	846	3214
Combined = $\lambda \cdot \epsilon \cdot \mu \cdot V_s \cdot E_c^2$	1	3.7	257627	248	353	37
Baliga High Frequency = $\mu \cdot E_c^2$	1	10.1	13333	46	100	142
Keyes = $\lambda \cdot [(c \cdot V_s) / (4\pi \cdot \epsilon)]^{1/2}$	1	0.3	23.0	3.6	1.8	0.2

Power semiconductor devices, used in three-terminal switches or two-terminal rectifiers, when forward biased should have minimal resistance in the on-state, R_{on-sp} , and support a large blocking voltage, V_B , in the off-state [3]. In a standard device design, increasing the thickness, L_N , or decreasing the doping, N_d , of an n⁻ drift region increases the on-resistance as described by

$$R_{on-sp} = \frac{L_N}{q\mu_n N_d} \quad (1)$$

Avalanche breakdown occurs when the electric field in the depletion region exceeds the material dependent critical value, E_c [4]. For an abrupt junction, the depletion layer extends almost entirely in the lightly doped side as described by

$$W_D = \sqrt{\frac{\epsilon_s V_B}{qN_d}}, \quad (2)$$

where ϵ_s is the permittivity [5]. The linearly decreasing field across the depletion layer has a maximum at the junction. For a drift layer thickness sufficient to support this depletion width, $L_N \approx W_D$, the maximum breakdown is set by critical electric field, $V_B = \frac{E_c W_D}{2}$.

Relating these equations gives the maximum blocking voltage inversely related to the doping density in drift layer by

$$V_B = \frac{\epsilon_s E_c^2}{2qN_d} \quad (3)$$

Again combining these equations shows the inherent tradeoff between on-resistance and blocking voltage

$$R_{on-sp} = \frac{4V_B^2}{\epsilon_s \mu_n E_c^3}, \quad (4)$$

where the denominator of the equation is the Baliga figure of merit [6]. The simplest method to break this design tradeoff is to move to a semiconductor material with a higher critical electric field (Fig. 1).

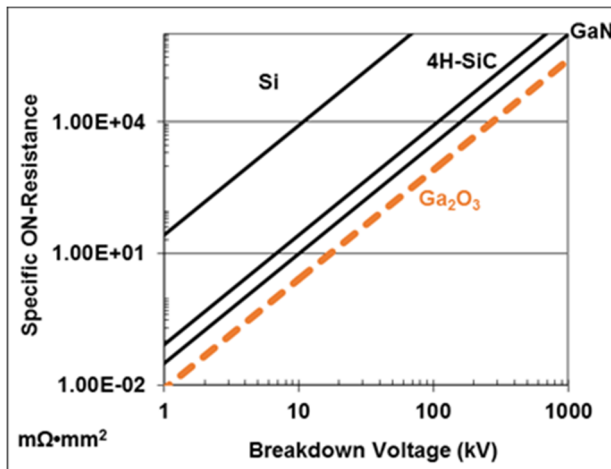


Fig. 1. Each material faces an inherent tradeoff of specific on-resistance to breakdown field as $R_{on-sp} \sim V_B^2$. The high critical electric field of Ga_2O_3 provides an inherent advantage compared to GaN and SiC given that $R_{on-sp} \sim E_c^{-3}$ [7].

Examination of the bandgap and breakdown field for various semiconductors reveals a simple relationship given by $\epsilon_c = a(E_g)^n$ where a and n are fitting parameters. Specifically, the parameters for indirect semiconductors are $a = 2.38 \times 10^5$ and $n = 1.995$, direct semiconductors are $a = 1.73 \times 10^5$ and $n = 2.506$, and all semiconductors are $a = 1.75 \times 10^5$ and $n = 2.359$ [8]. The generally accepted value for breakdown field of β -type of Ga_2O_3 is 8 MV/cm although this exceptionally high value has not been experimentally confirmed [9].

Early demonstrations of high-breakdown β - Ga_2O_3 electronic devices are promising, e.g., a critical field strength of 3.8 MV/cm and a 1kV vertical Schottky diode, yet fall short of the predicted levels. Several fundamental material issues are limiting the capability of β - Ga_2O_3 for power electronic devices. Experimental measurements of mobility are less

than half of the theoretical predictions. Key scattering mechanisms are still unclear including the role of point defects and defect complexes as well as structural stacking faults. Further studies are needed to understand the limitations in saturation electron velocity and breakdown field [9].

2. Crystal Structure of β -Ga₂O₃

Examining the structure of the β -Ga₂O₃ crystal helps to frame a number of issues in the growth and behavior of Ga₂O₃. The valence band maximum in β -Ga₂O₃ forms from weakly interacting O 2p orbital states with contribution of Ga 3d and 4s orbitals while the conduction band minimum forms from Ga 4s states [10]. Closer examination of Fig. 2 shows that the Ga³⁺ cations (with a green coloring) have two distinct bonding coordinations. The Ga (I) cation has a distorted tetrahedral coordination with four bonds and the Ga (II) cations has an octahedral coordination with six bonds. Among the common n-type dopants for β -Ga₂O₃, Si, and Ge donors prefer the tetrahedral coordination of the Ga(I) site while Sn donors prefer the octahedral coordination of Ga(II) Site.

Dramatic progress has been made over the past few years in the bulk crystal growth of β -Ga₂O₃. The edge-defined film-fed growth (EFG) technique involves pulling the boule along the [010] direction at a rate of approximately 15mm/hr. The EFG process has led to the production of up to 4-inch diameter Ga₂O₃ substrates oriented in ($\bar{2}01$) or (001) planes. The float zone technique is able to produce (100), (010), and (001) oriented boules with a diameter of 1 inch at a growth rate approaching 5mm/hr. The Czochralski technique has produced, at a pull rate of 2 mm/hr, (100) oriented boules of 2-inch diameter with potential for larger diameter boules in the future [11]. The dislocation density of current bulk wafers is of the order 10^3 cm⁻², a key result for making large area power devices [9].

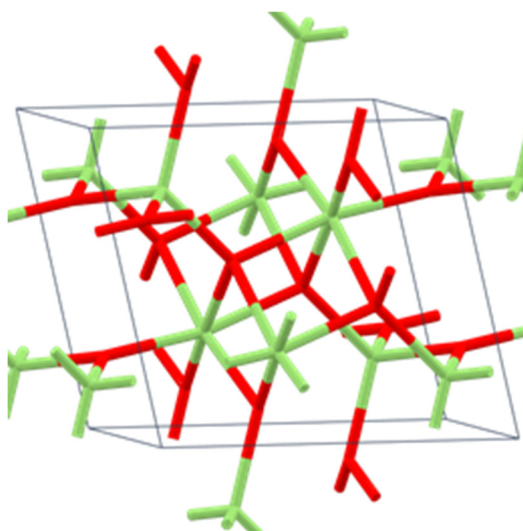


Fig. 2. Bonding structure of monoclinic (C2/M group symmetry) β -Ga₂O₃ phase.

3. Homoepitaxy on (100) Plane

The availability from the Czochralski process of (100) orientated wafers provided a basis for a series of homoepitaxial studies [12, 13] as described in [14]. Schewski et al. found that double positioning (180° rotation) of the monoclinic crystal growth (100) plane leads to twin lamellae formation and stacking mismatch boundaries. This double positioning creates a number of possible monoclinic Ga₂O₃ stacking faults including a half unit cell twin layer, a twin layer at surface, and diagonal stacking fault that serves to restore lattice stacking in the direction of growth [15].

Schewski et al. reported that (100) substrates offcut towards the [001] direction provided steps to align the crystal. The growth proceeds in a step-flow manner where impinging adatoms diffuse to a terrace edge. It was observed that an optimal miscut of 6° leads to a density of twins of approximately zero [15]. Conceptually it follows that too small of an offcut can lead to isolated nucleation of islands on large terraces with double positioning and resultant formation of twin lamellae and stacking mismatch boundaries.

In order to describe this process of adatom diffusion to step edges vs. formation of (potentially twinned) islands, Schewski et al. extended a model of Bales and Zangwill [16]. This model required the coupled solution to a set of ordinary differential equations ODEs for the density of adatoms, $\langle n_1 \rangle$,

$$\frac{1}{F} \frac{d\langle n_1 \rangle}{dt} = \gamma - \frac{D}{F} \xi^{-2} \langle n_1 \rangle - \frac{D}{F} \chi \langle n_1 \rangle - k_1 \langle n_1 \rangle - \sum_{s=1}^{\infty} k_s \langle n_s \rangle, \quad (5)$$

and density of island of size s, $\langle n_s \rangle$,

$$\frac{1}{F} \frac{d\langle n_s \rangle}{dt} = \frac{D}{F} \sigma_{s-1} \langle n_1 \rangle \langle n_{s-1} \rangle - \frac{D}{F} \sigma_s \langle n_1 \rangle \langle n_s \rangle + k_{s-1} n_{s-1} - k_s \langle n_s \rangle \quad s = 2, 3, \dots, \quad (6)$$

with equations for flux of incoming adatoms, F, adatom attachment, γ , diffusion to Island, ξ , diffusion to step edge, χ , and deposition on existing island detailed in [15]. The solution to these equations is displayed in Fig. 3 at four growth rates that define the adatom flux to the surface.

This calculation provides some guidance on how to control the stacking fault formation for homoepitaxy on (100) plane. Examination of Fig. 3 indicates that a layer with minimal stacking faults requires a flux of atoms to the surface in less than the time for these atoms to diffuse to a step edge. The diffusion constant of 7×10^{-9} cm²s⁻¹ employed in this calculation is based on a growth temperature of 850°C. Increasing the growth temperature is a clear lever to increase diffusion rate; however, decomposition of the surface is expected at higher temperatures. Nevertheless, reports of Si doping as well as In doping or (In_xGa_{1-x})₂O₃ alloy formation have shown a surfactant-mechanism that can increase the effective adatom diffusion rate [17].

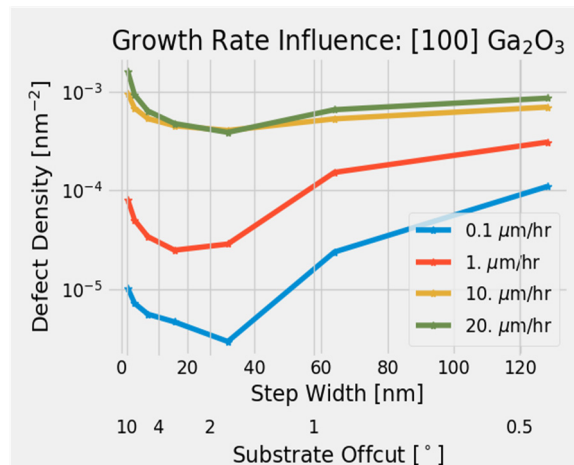


Fig. 3. Calculation of stacking fault density as a function of terrace step width for various growth rates. At low offcut, the adatom surface diffusion length is less than the step terrace width, which leads to island growth with twin and related stacking fault formation. In contrast, a step-bunching mechanism will occur at high offcut [15].

4. Facet Stability

A follow-on study by Schewski et al. found that the substrate monoclinic offcut direction of $[00\bar{1}]$ and $[001]$ were not equivalent [18]. A Ga_2O_3 substrate offcut towards $[00\bar{1}]$ resulted in steps that reconstruct as the $(\bar{2}01)$ facet. Subsequent deposition proceeded in a 2D step-flow manner and the resultant film had high mobility. In contrast, a Ga_2O_3 substrate offcut towards $[001]$ reconstructed as a twin $(\bar{2}01)$ defect nucleated at a $(001)\text{-B}$ step. The film deposited on this substrate possessed a high density of stacking faults (that behaved as acceptor-like electron trap states) and displayed low electron mobility.

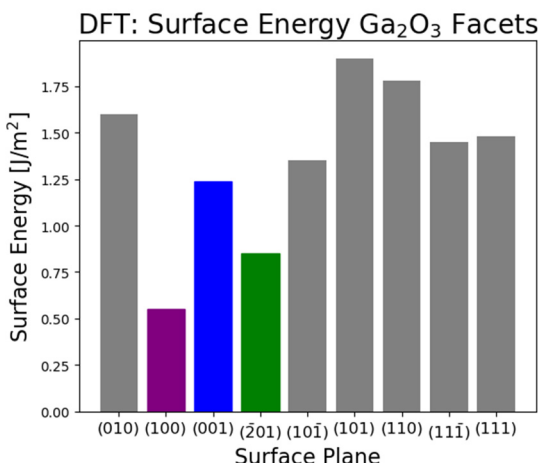


Fig. 4. Density functional theory calculation of surface energy of relevant Ga_2O_3 surfaces [18].

An earlier ab-initio studies by Bermudez reported a low surface energy of β -Ga₂O₃ on the (100) plane [19]. The general understanding of facet energetics was based on this report by Bermudez that only examined that the (100), (010), (001) and (101̄) faces of β -Ga₂O₃. The energy of these crystal planes is shown in Fig. 4 with the inclusion of the (201̄) plane [18]. The reconstruction of the {001} step edge for the <001> offcut is apparent given that the surface energy of the (201̄) plane is lower than the (001) plane. As discussed by Schewski et al., the asymmetry of the monoclinic (100) crystal results in an asymmetry of the reconstruction. Specifically the (001)-B step cannot form the (201̄) plane without a stacking fault [18].

Although the preceding discussion was based on homoepitaxy on (100) plane, it is clear that the crystal facet energetics determine the preferred orientations in bulk crystal growth (as discussed above) and the defect formation mechanisms of thin-film growth. Rafique et al. found that hetero-epitaxy on (0001) c-plane sapphire produced (201̄) oriented Ga₂O₃ with in-plane rotational domains. The use of (0001) sapphire offcut towards (1120̄) favored the formation of one domain with the highest mobility found for the film grown on (0001) sapphire with an offcut of 6° [20]. Another effect of the crystal facet energetics was seen in the surface morphology of homoepitaxy (010) Ga₂O₃, which formed with a striped surface morphology along [001] [21].

5. Carrier Concentration / Compensation

There has also been progress in the development in the epitaxy of doped β -Ga₂O₃ by a number of techniques, including MOCVD, HVPE, and MBE with reports of n-type doping over the range 10¹⁵ to 10¹⁹ cm⁻³ using Sn or Si shallow donors [9]. It is critical to understand the influence of precursor (trimethylgallium (TMGa) vs. triethylgallium (TEGa)), dopant type (Sn vs. Si) and carrier gas (Ar vs. N₂). This interplay in the growth environment can be expected given that in β -Ga₂O₃ the top of the valence and the bottom of the conduction band, respectively, are made up of the anionic (O 2p states with contributions from Ga 3d and 4s orbitals) and cationic states (Ga 4s states). Similarly, the carrier behavior has been shown to dramatically change under annealing, e.g., N₂ annealing creates deep acceptor states in n-type β -Ga₂O₃ [22, 23].

Figure 5 provides a comparison of conductivity for each particular set of precursor and dopant. Baldini et al. found in MOCVD efficient activation of the Si dopant to produce free carriers in the range of 1x10¹⁷ to 8x10¹⁹ cm⁻³ in β -Ga₂O₃ films on (010) β -Ga₂O₃ substrates [21]. In contrast, incorporation of the Sn dopant was hampered above a concentration of 1x10¹⁹ cm⁻³. This behavior is framed by the earlier discussion that Si (and Ge) prefer the tetrahedral coordination of Ga(I) site and Sn prefers octahedral coordination of Ga(II) site. Lastly, Baldini et al. reported that a memory effect of Sn in the reactor produced films with an unintentional Sn concentration of approximately 4x10¹⁷ cm⁻³ [21].

It is commonly understood for MOCVD of compound semiconductor films that the TMGa reaction pathway of $\text{Ga(CH}_3\text{)}_3 \rightarrow \text{Ga-CH}_2(\text{surface}) + \text{CH}_4(g)$ can leave a high level of carbon in the films. This is in contrast to the TEGa sequential β -elimination pathway of $\text{Ga(C}_2\text{H}_5\text{)}_3 \rightarrow (\text{C}_2\text{H}_5)_2\text{GaH} + \text{C}_2\text{H}_4(g)$ that should yield a semiconductor film with relatively

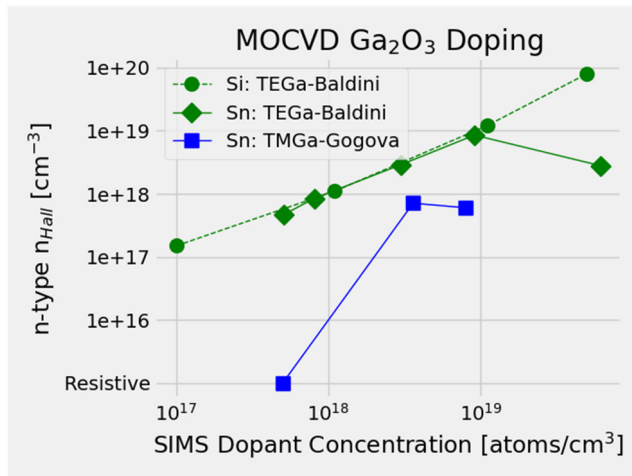


Fig. 5. Comparison of Si and Sn doping during growth of β - Ga_2O_3 with TMGa and TEGa precursors (adapted from [21] and [24]). With a TEGa source, moderate levels of Sn and Si dopant demonstrate linear n-type incorporation in β - Ga_2O_3 .

less carbon. Similarly it is generally understood in an MOCVD growth environment with a gallium metalorganic precursor that a decrease in growth temperature will increase the relative level of carbon, which may act as a deep acceptor. This may be especially pertinent given the deposition temperature of β - Ga_2O_3 is approximately 300 degrees lower than the typical MOCVD temperature for GaN. Additionally, an increase in growth rate will generally increase the relative level of carbon.

It has been generally observed that MOCVD films produced via a Ga source of TMGa are resistive except at high n-type doping and with H_2O as the oxygen source. Using TMGa and H_2O , Gogova et al. doped β - Ga_2O_3 with Sn on (0001) sapphire and (100) β - Ga_2O_3 substrates (Fig. 5). Raman spectroscopy of the films found C-H-related bands. Their analysis stated that Ga vacancy-related defects and the carbon-related complexes act as acceptors compensating for the Sn donors [24].

Tuomisto et al. employed positron annihilation spectroscopy to relate the concentration of negative and neutral vacancies to the conductivity of doped and undoped β - Ga_2O_3 thin films [25]. These results as depicted in Fig. 6 show that MOCVD with a Ga source of TEGa resulted in a low concentration of gallium vacancies while MOCVD with a TMGa precursor resulted in a high concentration of gallium vacancies. Not shown in the plot is that all films with a vacancy concentration equal to or greater than $1 \times 10^{17} \text{ cm}^{-3}$ were insulating. An interesting conclusion from Tuomisto et al. [25] is that growth kinetics and chemical reactions at the MOCVD growth surface dictate the Ga vacancy formation, i.e., not the Fermi level potential of the crystal in a thermodynamic equilibrium condition.

An underlying mechanism for unintentional conductivity in β - Ga_2O_3 was suggested to be based on hydrogen [26, 27]. Interstitial hydrogen (H_i) or hydrogen trapped at oxygen vacancies (H_o) is predicted to act as a shallow donors [9]. Qin et al. employed infrared

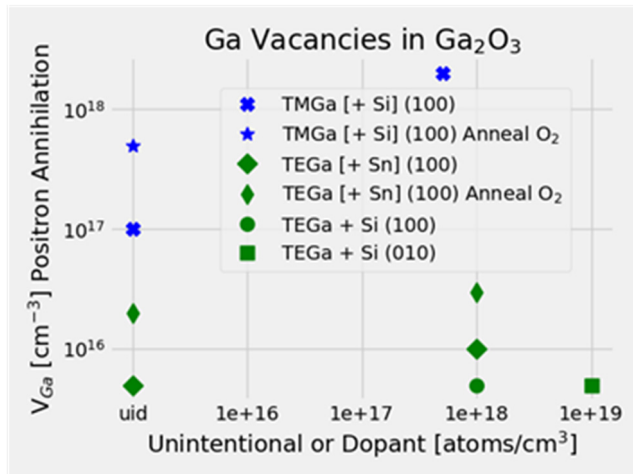


Fig. 6. Comparison of gallium vacancy, V_{Ga} , concentration as measured by positron annihilation spectroscopy as a function of dopant concentration for comparing TEGa and TMGa precursors as well as with and without an oxygen anneal (as adapted from [25]). All films deposited with a TMGa precursor displayed a vacancy concentration equal to or greater than $1 \times 10^{17} \text{ cm}^{-3}$ and were electrically insulating (not shown).

spectroscopy to study β - Ga_2O_3 annealed in a H_2 or D_2 ambient. This study found a hidden reservoir of hydrogen that is composed of various hydrogen centers coupled to a gallium vacancy as well as a variety of other species. Vibrational spectroscopy assigned the dominant hydrogen center to a neutral complex composed of two equivalent hydrogen at a relaxed gallium vacancy, $V_{\text{Ga(I)}}\text{-}2\text{H}$ [28].

6. Mobility Limits

The reported theoretical room temperature mobility of β - Ga_2O_3 is in the range of 200 to $300 \text{ cm}^2/\text{V}\cdot\text{s}$; however, typical experimental mobilities are reported in 50 to $150 \text{ cm}^2/\text{V}\cdot\text{s}$ range [9]. Referring to Table 1, the mobility of β - Ga_2O_3 is low relative to other wide bandgap semiconductors. It is constructive to understand what limits the electron mobility in the β - Ga_2O_3 crystal. As discussed by Ma et al., β - Ga_2O_3 has an effective mass, m_c^* , of approximately $0.25m_0$, which is comparable to the effective mass of GaN of $0.21m_0$ although the mobility of GaN is approximately $1200 \text{ cm}^2/\text{V}\cdot\text{s}$ [29].

It is known that the bonding of Ga and O has a large difference in electronegativity, X_{AB} , or similarly a large Pauling ionicity given by $f_P = 1 - \exp\left(\frac{-X_{AB}}{4}\right)$. A useful value for predicting the influence of electron to polar optical phonon interaction in polar semiconductors is the Fröhlich coupling constant,

$$\alpha_F = \frac{q^2}{8\pi\epsilon_0} \sqrt{\frac{2m_c^*}{\hbar\omega_0}} \left(\frac{1}{\epsilon_\infty} - \frac{1}{\epsilon_s} \right), \quad (7)$$

where $\hbar\omega_0$ is the polar optical phonon energy, ε_∞ and ε_s are the high- and low-frequency relative dielectric constants, and ε_0 is the vacuum permittivity. The Fröhlich coupling constant is quite large in $\beta\text{-Ga}_2\text{O}_3$ crystal as can be seen in Fig. 7.

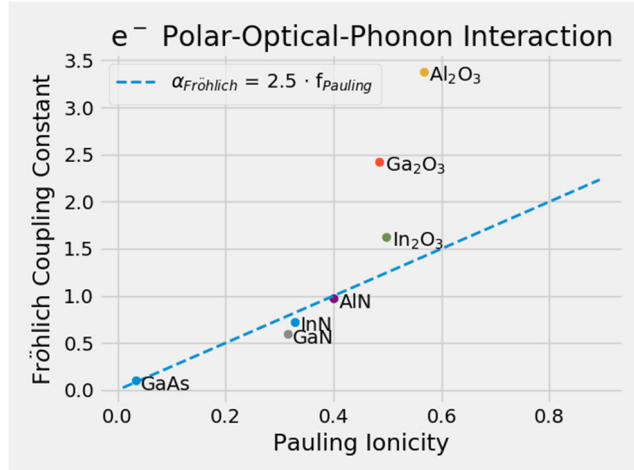


Fig. 7. The exceptionally strong electron to polar optical phonon interaction as measured by the dimensionless Fröhlich coupling constant in $\beta\text{-Ga}_2\text{O}_3$ greatly exceeds what would be expected from a naive linear prediction given the strong ionic character (as measured by the Pauling ionicity) in the Ga-O bond [29].

The mobility in semiconductors is controlled by several scattering mechanisms with one mechanism usually dominant for a given set of dopant levels and temperature. It is common in polar semiconductors at room temperature for phonon scattering to limit the mobility at low donor levels while impurity scattering limits the mobility at high impurity levels. The impact of the predicted large Fröhlich coupling constant is apparent in Fig. 8a, which displays the mobility of $\beta\text{-Ga}_2\text{O}_3$ as a function of doping. It is clear in Fig. 8a that the electron scattering by polar optical phonons limits the mobility to approximately $200 \text{ cm}^2/\text{V}\cdot\text{s}$ for $\beta\text{-Ga}_2\text{O}_3$ with donor densities less approximately $5 \times 10^{18} \text{ cm}^{-3}$.

Examining the mobility at a low donor level in Fig. 8b reveals that electron mobility is controlled by polar optical phonon scattering at temperatures above 200K. The general understanding of semiconductor transport is that phonon scattering is inherent to the particular crystal and only marginal improvement may be possible through strain engineering [30].

In contrast, the mobility at a donor level of $1 \times 10^{20} \text{ cm}^{-3}$ is depicted in Fig. 8c. As mentioned above, neutral and ionized impurity scattering dominates at above approximately $5 \times 10^{18} \text{ cm}^{-3}$. In Fig. 8c, the high donor level leaves a large density of neutral impurities that are the dominant scattering source in the temperature range depicted.

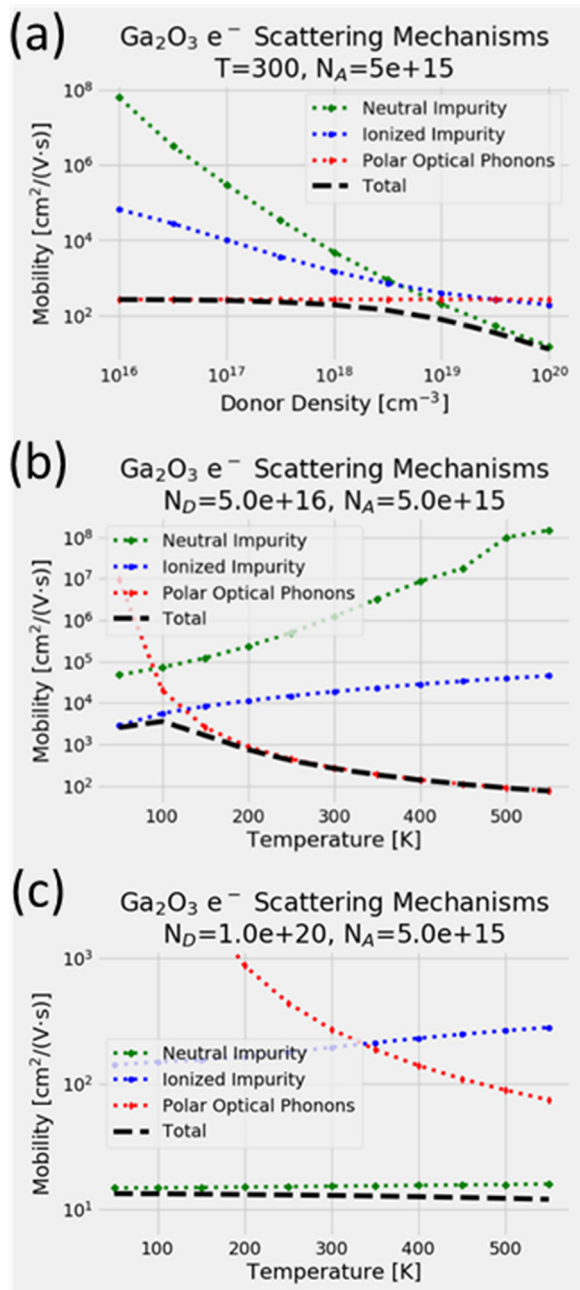


Fig. 8. Calculated mobility and relevant scattering mechanisms in β -Ga₂O₃ (a) at 300K as a function of donor density, (b) as a function of temperature at a low donor level (5×10^{16} cm⁻³) where polar optical phonon scattering is the dominant mechanism limiting the mobility above 200K, and (c) as a function of temperature at a high donor level (1×10^{20} cm⁻³) where impurity scattering controls the mobility.

The strong influence of neutral and ionized impurity scattering at high doping levels motivated the development of modulation doped heterostructures where the donor source and the transport channel are physically displaced. This design is the basis of the well-known modulation doped field effect transistor (MODFET). This structure is depicted in Fig. 9a, where donors in the delta doped portion of the $(\text{Al}_x\text{Ga}_{1-x})_2\text{O}_3$ barrier are physically displaced from the conductive channel formed in a triangular potential well at the $(\text{Al}_x\text{Ga}_{1-x})_2\text{O}_3/\text{Ga}_2\text{O}_3$ interface.

A key design criteria in MODFETs is the physical spacing between the two-dimensional electron gas in the channel and the delta doped layer. As is visible in Fig. 9a, the electron wavefunction for the conductive channels extends to the donors in the delta-doped barrier. This provides a mechanism for screening of the electrons in the channel by neutral and ionized donors in the barrier. This confinement of carriers is further improved by increasing the aluminum composition in the barrier to increase the conduction band offset between $(\text{Al}_x\text{Ga}_{1-x})_2\text{O}_3$ and Ga_2O_3 . An additional bandgap engineering constraint is to prevent the formation of a second conductive channel at the delta-doped layer in the barrier.

As discussed earlier, polar optical phonon scattering creates a fundamental limitation that is difficult to mitigate in the mobility of polar semiconductors. Ghosh and Singisetti recently made a dramatic prediction of a screening mechanism for polar optical phonons in Ga_2O_3 [32]. It is known that a 2D electron gas in a semiconductor behaves at a plasmon wave with a characteristic energy defined by the density of electrons [31]. Ghosh and Singisetti studied how this plasmon wave couples to the longitudinal optical phonon modes in Ga_2O_3 . This remarkable study found that at moderate electron densities the plasmon wave will anti-screen the longitudinal optical phonons, which increases the scattering rate; while at high electron densities the plasmon wave will screen the longitudinal optical phonons, which decreases the scattering rate [32].

This anti-screening/screening behavior is observable in the dot-dashed line in the mobility vs. channel density plot in Fig. 9b. Dramatic improvements in mobility are predicted at electron densities above $5 \times 10^{18} \text{ cm}^{-3}$. Unfortunately, uniformly doping a single epilayer to achieve these carrier densities will create a high density of impurity scattering sites that will severely limit the mobility as was discussed for Fig. 8. Again the solution is to separate the dopants from 2D electrons. Still, the electrons in the triangular potential well can experience scattering by the donors in the delta-doped layer. The mobility accounting for the anti-screening/screening behavior as well as the scattering by the remote impurities is displayed by the dashed line in Fig. 9b. As can be seen, there is a clear design tradeoff to minimize the impurity scattering sites vs. increasing the channel density to increase the polar optical phonon screening - as well as standard MODFET design rules [4, 33, 34].

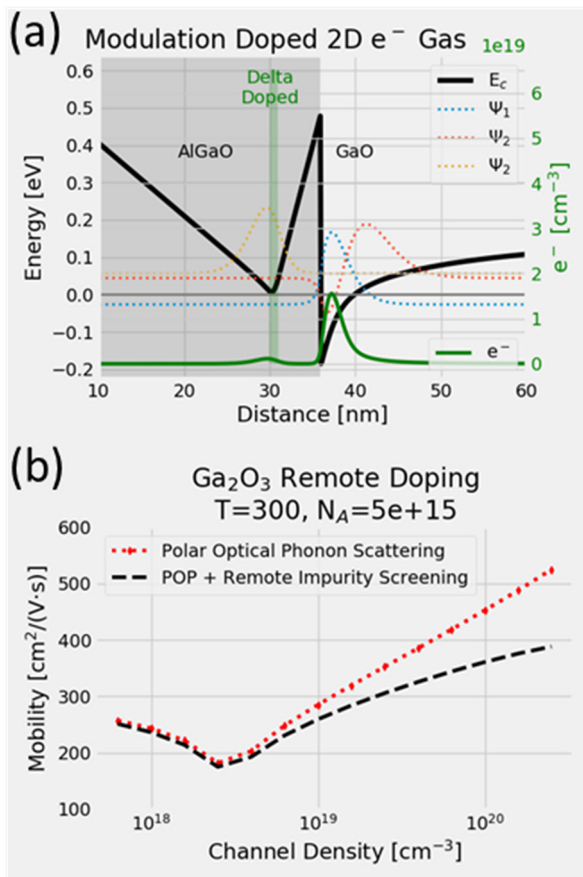


Fig. 9. β -($\text{Al}_{x}\text{Ga}_{1-x}\text{O}_3$)/ Ga_2O_3 modulation doped structure with a conductive channel formed in a triangular potential well. (a) Calculation of conduction band energy, electron concentration, and electron wavefunction for a structure composed of 35nm delta-doped ($\text{Al}_{x}\text{Ga}_{1-x}\text{O}_3$) on Ga_2O_3 . A small portion of the electron wavefunction in the channel extends to the delta-doped donors in the ($\text{Al}_{x}\text{Ga}_{1-x}\text{O}_3$) layer. (b) The dot-dashed line depicts a mobility model that accounts for polar optical phonon anti-screening at moderate electron densities and screening at high electron densities [32]. The dashed line depicts the mobility including screening by the remote impurities in the delta-doped layer.

7. Alloy Formation

From the previous section it is clear that research is needed in epitaxy of ($\text{Al}_{x}\text{Ga}_{1-x}\text{O}_3$)/ Ga_2O_3 heterostructures. The ($\text{Al}_{x}\text{Ga}_{1-x}\text{O}_3$) alloy is challenging as α - Al_2O_3 is stable as the corundum phase (Fig. 10) while β - Ga_2O_3 is stable as the monoclinic phase.

The phase of ($\text{Al}_{x}\text{Ga}_{1-x}\text{O}_3$) that forms not only has a different bandgap energy but presents a different transition state. It is known that the β - Ga_2O_3 is theoretically an indirect semiconductor but this direct gap transition is so similar in energy that β - Ga_2O_3 effectively behaves as a direct gap semiconductor. Examination of Fig. 11, which is based on the model in Peelaers, et al. [35], shows that the energy difference of the indirect transition

compared to the direct transition increases to a significant level with increasing alloy composition. The influence of this effect on device properties is not well studied. Similarly, the separation of the indirect and direct transition energies in the $(\text{Al}_x\text{Ga}_{1-x})_2\text{O}_3$ corundum phase is also shown in Fig. 11.

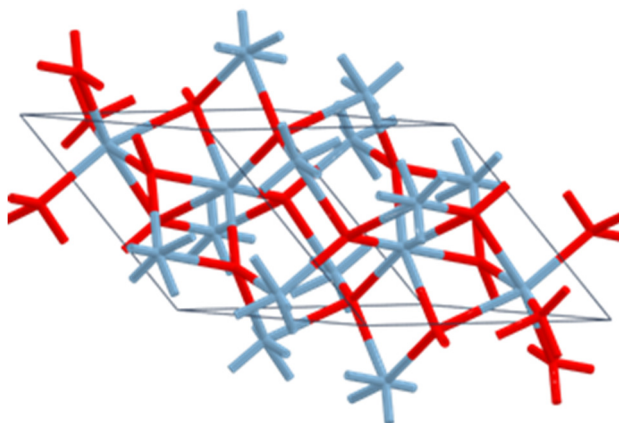


Fig. 10. Bonding structure of the stable corundum $\alpha\text{-Al}_2\text{O}_3$ (R3c group symmetry) phase where the Al cations are octahedral coordinated with six bonds.

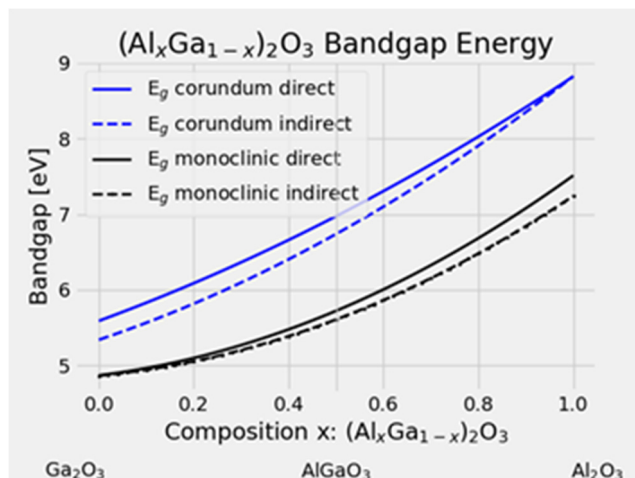


Fig. 11. Direct and indirect bandgap energies of the monoclinic and corundum phases of the $(\text{Al}_x\text{Ga}_{1-x})_2\text{O}_3$ alloy [35].

It is known that forming alloys of $(\text{Al}_x\text{Ga}_{1-x})_2\text{O}_3$ is difficult. Examination of Fig. 12 based on the enthalpy of formation model of Peelaers, et al. [35] provides some insight. The calculation suggests that the monoclinic phase is stable for $x < 0.71$. The stability local minimum in the formation energy for AlGaO_3 ($x = 0.5$) is logical given the crystal structure

of the binary compounds. The bonding structure of the corundum α -Al₂O₃ phase is composed of Al cations only at octahedral coordinated sites with six bonds each (Fig. 10). In contrast, Fig. 2 shows that the monoclinic β -Ga₂O₃ phase is composed of equal parts of Ga (I) cations in a distorted tetrahedral coordination with four bonds and Ga (II) cations in an octahedral coordination with six bonds. At the stability local minima at $x = 0.5$, the Ga (I) cations are at the tetrahedral coordinate site while, critically, the Al cations are only present at the octahedral coordination site.

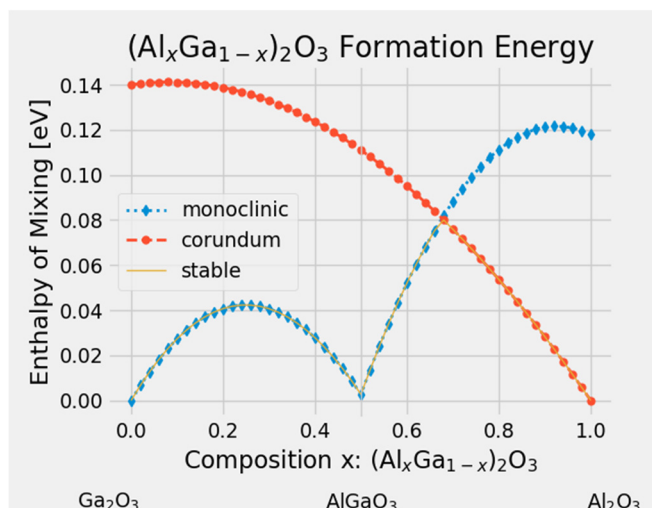


Fig. 12. Theoretical formation energy of $(\text{Al}_x\text{Ga}_{1-x})_2\text{O}_3$ based on the model of Peelaers, et al. [35]. The monoclinic phase is stable for $x < 0.71$ and the corundum phase is stable at higher mole fractions.

Early work by Hill et al. into the equilibrium diagram of Al₂O₃ in β -Ga₂O₃ found the presence of a stable phase of AlGaO₃ [36]. This work reported that this phase required a temperature of 800 °C, which may preclude lower temperature growth techniques such as MBE. The exploration of AlGaO₃ growth conditions and the role of strain is an important area of future research.

The addition of $(\text{In}_x\text{Ga}_{1-x})_2\text{O}_3$ to heterostructures would also be beneficial for the development of electronic devices. Again, the In₂O₃ crystal possesses a different stable phase (as seen in Fig. 13), which contributes to the difficulty in forming a $(\text{In}_x\text{Ga}_{1-x})_2\text{O}_3$ stable alloy. Single crystal monoclinic structures were only reported at low indium content ($x < 0.15$). At high indium content ($x > 0.8$) the cubic bixbyite phase is formed while at intermediate values an additional rhombohedral InGaO₃(II) crystallographic phase formed [37]. Regardless, as discussed above, reports indicate that indium behaves as a surfactant so its key role may be in improving the diffusivity of the gallium atom during growth.

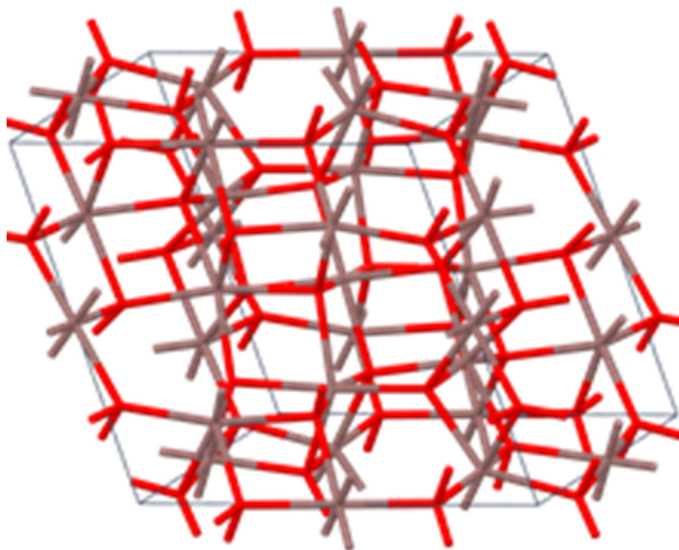


Fig. 13. Bonding structure of the stable cubic bixbyite In_2O_3 ($\text{Ia}=3$ [206]) group symmetry phase with the In cations in an octahedral coordination with six bonds.

8. Conclusion

Development of β - Ga_2O_3 -based MOCVD technology will enable power electronic devices not possible with other semiconductor materials. The energetics of the crystal facets has a strong influence on growth morphology and defect formation for a given substrate orientation and offcut, growth temperature, and growth rate. It is clear that the growth environment, particularly metalorganic precursor selection and the presence of hydrogen, has a strong impact on the formation of gallium vacancies and the resulting compensation of intentional dopants. These compensating centers may be native defects or complexes from either sublattice. The understanding of the role of hydrogen including in the formation the vacancy complex is still evolving. The mobility in β - Ga_2O_3 is limited at low donor densities by polar optical phonons. The possibility to screen the longitudinal optical phonon modes by the electron gas plasmon further motivates development of modulation doped $(\text{Al}_x\text{Ga}_{1-x})_2\text{O}_3/\beta\text{-Ga}_2\text{O}_3$ heterostructures. To achieve efficient devices based on this structure requires additional development into the growth of $(\text{Al}_x\text{Ga}_{1-x})_2\text{O}_3$ particularly at high alloy mole fraction.

Acknowledgments

The work at NRL was partially supported by DTRA Grant No. HDTRA1-17-1-0011 (Jacob Calkins, monitor) and the Office of Naval Research. The work at UF is partially supported by HDTRA1-17-1-0011. The project or effort depicted is sponsored by the Department of the Defense, Defense Threat Reduction Agency. The content of the information does not necessarily reflect the position or the policy of the federal government, and no official

endorsement should be inferred. The work at Korea University was supported by the Korea Institute of Energy Technology Evaluation and Planning (KETEP) and the Ministry of Trade, Industry and Energy (MOTIE) of Korea (Grant No. 20172010104830) and Space Core Technology Development Program (2017M1A3A3A02015033) through the National Research Foundation of Korea funded by the Ministry of Science, ICT and Future Planning of Korea.

References

1. M.A. Mastro, A. Kuramata, J. Calkins, J. Kim, F. Ren, S.J. Pearton, ECS J. Solid State Sci. Technol. 6, P356 (2017)
2. B.J. Baliga, IEEE Electron Device Letters, 10, 455 (1989)
3. S. Dimitrijev, J. Han, D. Haasmann, H.A. Moghadam, and A. Aminbeidokhti, , MRS Bulletin 40(05), 43-46 (2014)
4. S.S. Li, Semiconductor Physical Electronics, Plenum (1993)
5. S. Dimitrijev, Principles of Semiconductor Devices, Second Edition, New York, Oxford: Oxford University Press (2012)
6. B.J. Baliga, J. Appl. Phys. 53, 1759 (1982)
7. M.A. Mastro, Power MOSFETs and Diodes. In S. Pearton, F. Ren, M. Mastro (Eds.) Gallium Oxide Technology, Devices and Applications, p. 401-418, Elsevier (2019)
8. M.A. Mastro, Fundamentals and future of semiconductor device technology in III-V Compound Semiconductors: Integration with Silicon-Based Microelectronics, CRC/Taylor & Francis (2011)
9. S.J. Pearton, J. Yang, P.H. Cary, F. Ren, J. Kim, M.J. Tadjer, M.A. Mastro, Appl. Phys. Rev. 5, 011301 (2018)
10. H. Peelaers, C.G. Van de Walle, Phys. Rev. B 94, 195203 (2016)
11. Z. Galazka, R. Uecker, D. Klimm, K. Irmscher, M. Naumann, M. Pietsch, A. Kwasniewski, R. Bertram, S. Ganschow, M. Bickermann, ECS J. Solid State Sci. and Tech., 6(2), q3007 (2017)
12. A. Fiedler, R. Schewski, M. Baldini, Z. Galazka, G. Wagner, M. Albrecht, K. Irmscher, Applied Physics 122, 165701 (2017)
13. R. Schewski, G. Wagner, M. Baldini, D. Gogova, Z. Galazka, T. Schulz, T. Remmele, T. Markurt, Holger von Wenckstern, M. Grundmann, O. Bierwagen, P. Vogt, M. Albrecht, Appl. Phys. Express 8, 011101 (2015)
14. R. Fornari, Progress in MOVPE growth of Ga₂O₃. In S. Pearton, F. Ren, M. Mastro (Eds.) Gallium Oxide Technology, Devices and Applications, p. 3-30, Elsevier (2019)
15. R. Schewski, M. Baldini, K. Irmscher, A. Fiedler, T. Markurt, B. Neuschulz, T. Remmele, T. Schulz, G. Wagner, Z. Galazka, M. Albrecht, J. Applied Physics, 120(22), 225308 (2016)
16. G. Bales, A. Zangwill, Phys. Rev. B, 41, 5500 (1989)
17. M. Baldini, M. Albrecht, D. Gogova, R. Schewski, G. Wagner, Semi. Sci. and Tech. 30 (2), 024013 (2015)
18. R. Schewski, K. Lion, A. Fiedler, C. Wouters, A. Popp, S. V. Levchenko, T. Schulz, M. Schmidbauer, S. Bin Anooz, R. Grüneberg, Z. Galazka, G. Wagner, K. Irmscher, M. Scheffler, C. Draxl, M. Albrecht, APL Materials, 7(2), 022515 (2019)
19. V.M. Bermudez, Chem. Phys. 323, 193 (2006)
20. S. Rafique, L. Han, A. T. Neal, S. Mou, J. Boeckl, H. Zhao, Phys. Status Solidi A 215, 1700467 (2017)

21. M. Baldini, M. Albrecht, A. Fiedler, K. Irmscher, R. Schewski, G. Wagner, ECS J. Solid State Sci. Technol. 6, Q3040 (2017)
22. A. Kuramata, K. Koshi, S. Watanabe, Y. Yamaoka, T. Masui, S. Yamakoshi, Jpn. J. Appl. Phys. 55, 1202A2 (2016)
23. O. Ueda, N. Ikenaga, K. Koshi, K. Iizuka, A. Kuramata, K. Hanada, T. Moribayashi, S. Yamakoshi, and M. Kasu, Jpn. J. Appl. Phys. 55, 1202BD (2016)
24. D. Gogova, M. Schmidbauer, A. Kwasniewski, CrystEngComm 17-35, (2015)
25. F. Tuomisto, A. Karjalainen, V. Prozheeva, I. Makkonen, G. Wagner, M. Baldini, Proc. SPIE 10919, 1091910-1 (2019)
26. M.R. Lorenz, J.F. Woods, R.J. Gambino, J. Phys. Chem. Solids, 28, 403 (1967).
27. J.B. Varley, J.R. Weber, A. Janotti, C.G. Van de Walle, Appl. Phys. Lett., 97, 142106 (2010)
28. Y. Qin, M. Stavola, W. Beall Fowler, P. Weiser, S.J. Pearton, ECS J. Solid State Sci. Technol. 8-7, Q3103 (2019)
29. N. Ma, N. Tanen, A. Verma, Z. Guo, T. Luo, H. (Grace) Xing, D. Jena, Appl. Phys. Lett., 109, 212101 (2016)
30. K.A. Khair, S.S. Ahmed, 2017 IEEE 17th International Conference on Nanotechnology (IEEE-NANO) (2017)
31. M. A. Mastro, ECS Journal of Solid State Science and Technology, 6 (11) S3044 (2017)
32. K. Ghosh, U. Singisetti, J. Mater. Res. 32-4142 (2017)
33. M.A. Mastro, J.R. LaRoche, N.D. Bassim, C.R. Eddy, Jr., Microelectronics Journal, 36, 705 (2005)
34. M.A. Mastro, D.V. Tsvetkov, V.A. Soukhovoev, A. Usikov, V. Dmitriev, B. Luo, F. Ren, K.H. Baik, S.J. Pearton, Solid State Electronics, 48, 179 (2004)
35. H. Peelaers, J.B. Varley, J.S. Speck, C.G. Van de Walle, Appl. Phys. Lett. 112, 242101 (2018)
36. V.G. Hill, R. Roy, and E.F. Osborn, J. Am. Ceram. Soc. 35, 135 (1952)
37. H. von Wenckstern, D. Splith, M. Purfürst, Z. Zhang, Ch. Kranert, S. Müller, M. Lorenz, M. Grundmann, Semicond. Sci. Technol. 30, 024005 (2015)